

Experimental and numerical analysis of hovering multicopter performance in low-Reynolds number conditions

*Original*

Experimental and numerical analysis of hovering multicopter performance in low-Reynolds number conditions / Carreno Ruiz, M.; Scanavino, M.; D'Ambrosio, D.; Guglieri, G.; Vilardi, A.. - In: AEROSPACE SCIENCE AND TECHNOLOGY. - ISSN 1270-9638. - ELETTRONICO. - (2022), p. 107777. [10.1016/j.ast.2022.107777]

*Availability:*

This version is available at: 11583/2970369 since: 2022-09-23T17:01:59Z

*Publisher:*

Elsevier

*Published*

DOI:10.1016/j.ast.2022.107777

*Terms of use:*

This article is made available under terms and conditions as specified in the corresponding bibliographic description in the repository

*Publisher copyright*

Elsevier preprint/submitted version

Preprint (submitted version) of an article published in AEROSPACE SCIENCE AND TECHNOLOGY © 2022,  
<http://doi.org/10.1016/j.ast.2022.107777>

(Article begins on next page)

# Experimental and Numerical Analysis of Hovering Multicopter Performance in Low-Reynolds Number Conditions

M. Carreño Ruiz <sup>\*</sup>, M. Scanavino <sup>†</sup>, D. D'Ambrosio <sup>‡</sup> and G. Guglieri <sup>§</sup>

*Department of Mechanical and Aerospace Engineering, Politecnico di Torino, Torino, 10124, Italy*

A. Vilardi <sup>¶</sup>

*terraXcube, Eurac Research, Bolzano, 39100, Italy*

Unmanned Aircraft Systems (UAS) are state of the art in the aerospace industry and are involved in many operations. Although initially developed for military purposes, commercial applications of small-scale UAS, such as multicopters, are abundant today. Accurate engineering tools are required to assess the performance of these vehicles and optimize power consumption. The thrust and power curves of the rotors used by small-scale UAS are essential elements in designing efficient aircraft. The scarcity of experimental data and sufficiently accurate prediction models to evaluate rotor aerodynamic performance in the flight envelope are primary limitations in UAS science. In addition, for small-scale rotors at usual rotation rates, chord-based Reynolds numbers are typically smaller than 100,000, a flow regime in which performance tends to degrade. In this paper, experimental data on small-scale multicopter propulsion systems are presented and combined with a Computational Fluid Dynamics (CFD) model to describe the aerodynamics of these vehicles in low Reynolds numbers conditions. We use the STAR-CCM+ software to perform CFD simulations adopting both a dynamic-grid, time-accurate analysis and a static-grid, steady-state technique that solves the Navier-Stokes equations in a suitable framework. Comparing numerical simulation results on a conventional UAS propeller with related experimental data suggests that the proposed approach can correctly describe the thrust and torque coefficients in the range of Reynolds numbers characterizing the UAS flight envelope.

## Nomenclature

---

<sup>\*</sup>PhD Student, Department of Mechanical and Aerospace Engineering, Politecnico di Torino, C.so Duca degli Abruzzi, 24, 10124 Torino, Italy, manuel.carreno@polito.it

<sup>†</sup>PhD, Department of Mechanical and Aerospace Engineering, Politecnico di Torino, C.so Duca degli Abruzzi, 24, 10124 Torino, Italy, matteo.scanavino@polito.it

<sup>‡</sup>Adjunct Professor, Department of Mechanical and Aerospace Engineering, Politecnico di Torino, C.so Duca degli Abruzzi, 24, 10124 Torino, Italy, domenico.dambrosio@polito.it

<sup>§</sup>Full Professor, Department of Mechanical and Aerospace Engineering, Politecnico di Torino, C.so Duca degli Abruzzi, 24, 10124 Torino, Italy, giorgio.guglieri@polito.it

<sup>¶</sup>PhD, Senior researcher at terraXcube, Eurac Research, Via Ipazia, 2, 39100, Bolzano, Italy, andrea.vilardi@eurac.edu

$C_Q = \frac{Q}{\rho\pi\Omega^2 R^5}$	= rotor torque coefficient
$C_T = \frac{T}{\rho\pi\Omega^2 R^4}$	= rotor thrust coefficient
$C_P = \frac{P}{\rho\pi\Omega^3 R^5}$	= rotor power coefficient
$FM$	= rotor figure of merit
$D$	= rotor diameter
$\Omega$	= rotation rate in radians per second
$RPM$	= rotation rate in revolutions per minute
$R$	= rotor radius
$c$	= chord length at 75% radial station
$Re = \frac{0.75\rho\Omega Rc}{\mu}$	= rotor Reynolds number computed at the 75% radial station
$M$	= rotor tip Mach number
$T$	= rotor thrust
$Q$	= rotor torque
$P$	= rotor power
$\rho$	= air density
$\gamma$	= intermittency
$k$	= turbulent kinetic energy
$Re_\theta$	= momentum thickness Reynolds number
$\omega$	= specific dissipation rate

## I. Introduction

UNMANNED Aircraft Systems (UAS) have become popular vehicles in the last few years for recreational and commercial applications. Among all the types of UAS, small-scale rotary-wing UAS, particularly multicopter rotorcraft, offer great potential in many scenarios, such as earthquakes, floods, and avalanches. The Mars Helicopter *Ingenuity*, recently launched by NASA [1], is an example of the role played by UAS in complex scenarios. The flexibility of small UAS combined with emerging Artificial Intelligent (AI) tools makes these innovative vehicles suitable for dangerous applications to support and partially replace piloted aircraft.

While the design of multicopter UAS, as well as autopilot control laws, have been extensively studied in the literature [2–5], few research studies focus on the experimental characterization of small-scale vehicles providing details on their thrust and power consumption capabilities, especially when unconventional atmospheric conditions intervene, such as low density at high altitudes. The relatively small rotor size used by lightweight multicopter platforms, combined with relatively low rotation rates to avoid high tip Mach numbers, are responsible for low Reynolds numbers resulting in

laminar separation conditions that affect vehicle performance [6].

Brandt and Selig[7, 8] conducted the first studies on the effects of low Reynolds number on rotors for small-scale UAS by focusing on the isolated propulsion system rather than the complete vehicles. Their work has allowed measuring thrust and power coefficients for a range of rotors at Reynolds numbers less than 100,000. More recently, wind tunnel tests on small scales UAS were performed in 2016 at NASA Ames Research Center by Russell et al.[9]. The objective of that study was to collect a high-quality set of data related to multicopters in windy conditions. The authors took advantage of the U.S. Army 7'-by-10' wind tunnel to measure the thrust, torque, motor speed, and electrical power of a lightweight multicopter in the presence of different wind speeds and by varying the aircraft attitude in the test section. As part of their research, the authors studied the complete vehicle and isolated rotor performance to create a high-quality database for UAS development. A noticeable contribution was the geometrical characterization of rotors used by some of these vehicles exploiting a 3D laser scanner analysis [10]. These data are valuable for validating numerical tools for rotor performance predictions. We are unaware of systematic studies regarding the performance of UAS under unconventional atmospheric conditions (i.e., high altitude and temperature testing). Therefore, our data provide further information for understanding the aerodynamics of UAS platforms.

Mathematical tools used to evaluate rotor performance, such as Blade Element Momentum Theory (BEMT), can't fully describe the effects of small scale rotor aerodynamics in hovering, mainly due to the lack of wake modeling as shown by the authors in [11] comparing BEMT local thrust predictions with CFD and Free Vortex Wake simulations for isolated hovering rotors. Another Reduced Order Model (ROM), the Vortex Particle Method, has been employed by [12] to compute isolated rotor and multirotor aerodynamics. ROMs present the complication of requiring a high fidelity two-dimensional aerodynamic database for the different airfoils forming the rotor, which are difficult to obtain in this transitional range. Computational Fluid Dynamics (CFD) provides a way to improve predictions on both rotor and vehicle performance, avoiding the previously mentioned limitation but at a much higher computational cost. We propose an Unsteady Reynolds Averaged Navier Stokes (URANS) approach combined with a transition model in our CFD simulations. This strategy offers a compromise solution between ROMs and high fidelity scale resolving simulations such as those presented by [13] in the context of Urban Air Mobility (UAM). The main objective of the following study is to collect experimental data on small-scale multicopters and develop a CFD model able to describe precisely the flow around rotors, providing accurate performance predictions at a reasonable computational cost. In Section II we will provide details of the experimental activity that took place in a climate-controlled laboratory. The measured data include thrust, torque, and power coefficients for different Reynolds numbers considering unconventional atmospheric conditions, i.e., low temperature and high altitude which generate very low rotor Reynolds numbers and allows the study of the performance deterioration shown in [6]. Section III contains a description of the CFD model and its results, including comparisons with experimental data. For comparison between experimental data and CFD results, we used the T-Motor 15x5 propeller, typical of conventional multicopters involved in aerial surveillance operations. In section

IV we focus on validating and calibrating the above CFD tools based on experimental data collected on a complete small UAS and its propulsion systems. Finally, in section V, we draw the main conclusions of this research activity and indicate the guidelines for our future work.

## II. Experimental tests on small-scale UAS

terraXcube, managed by EURAC Research, is an infrastructure for research and testing that centers on the concept of cubes. The Large Cube, the Small Cube, and the Mini Cube, are three distinct chambers for an environmental simulation that enable a broad spectrum of experiments and tests [14–16]. We carried out aerodynamics experiments on rotary-wing vehicles in the Large Cube chamber, where it is possible to simulate the most extreme environmental conditions on the Earth’s surface. The Large Cube has a usable volume of  $360 \text{ m}^3$  and allows the synchronous control of multiple complex environmental parameters for long-duration analysis. The facility is fully re-configurable to perform industrial tests. We measured the aerodynamic performance of small-scale UAS on both an isolated rotor and the complete vehicle, considering combinations of temperature and altitude to explore their effects on thrust and power coefficients [17–20]. We describe the experimental setup and the main results in the following paragraphs. The authors will like to point out that, even though results from this experimental campaign have been partially previously published, this paper presents the final results of a series of experiments consolidating a definitive data set for validation purposes.

### A. Test matrix

Throttle, temperature, and altitude (via pressure) are the three independent variables that define our test matrix. Changing their value, one can generate a wide variety of Reynolds numbers, which, according to the dimensional analysis, along with the Mach number, are the only independent parameters affecting the thrust and torque coefficients of the hovering rotor. In any case, the small variation range of the tip Mach number and the vicinity to the incompressible limit makes its expected influence limited compared to the Reynolds number. The Prandtl-Glauert correction, shown in [21], could be employed using the Mach number at the tip to estimate the influence of compressibility effects on thrust and torque coefficients. This provides maximum differences of 3% in the range of Mach numbers shown in table 1. However, in the light of the radial thrust and torque distributions for this rotor shown in [11] and considering a linear dependency of Mach number with the radial coordinate, the estimated value would be conservative. A more accurate estimation is obtained by integrating the radial distributions corrected with Prandtl-Glauert’s approach. This technique produces maximum differences related to the Mach number of around 1.5% between the largest and smallest Mach numbers shown in table 1. Therefore, the Mach number effect is approximately an order of magnitude lower than the Reynolds number effect, which is responsible for variations of over 10% of the thrust coefficient in the considered ranges. We defined four throttle levels (50%, 66%, 86% and 100% of the maximum throttle), five temperature values (from  $40^\circ\text{C}$  to  $-40^\circ\text{C}$  in  $20^\circ\text{C}$  intervals), and six altitude conditions (from sea level to 6000 m in intervals of 1500 m with

a final test at 9000 m). This test matrix results in 120 cases which comprise a range of Reynolds numbers between 24,099 and 186,670. For the comparison and validation with numerical simulations, we chose three representative conditions as shown in table 1.

Reynolds number	Pressure(Pa)	Temperature(°C)	RPM	Tip Mach number
24,099	30,900	40.05	3293	0.19
61,539	58,000	19.91	3979	0.23
186,670	98,450	-40.85	4683	0.31

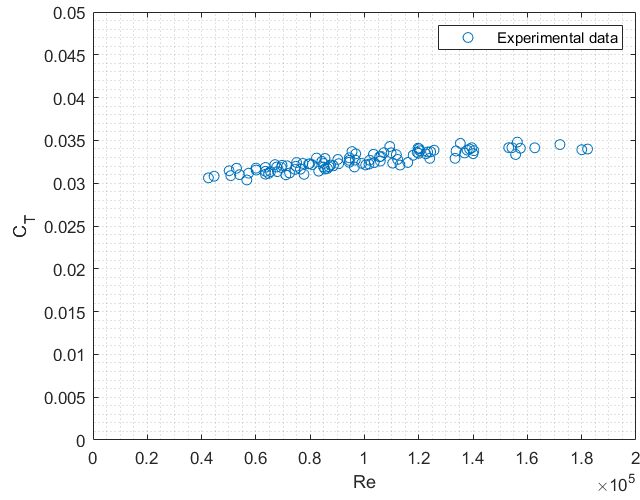
**Table 1 The three experimental conditions used for comparison with numerical simulations.**

## B. Experimental setup for small scale UAS testing

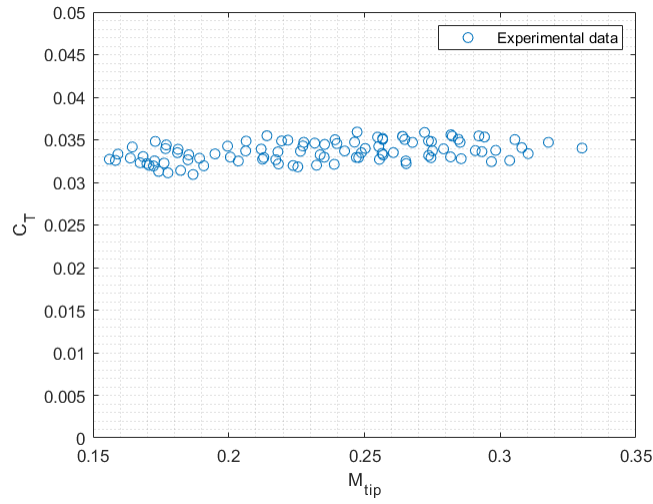
The test bench consists of a welded-steel construction with a central hollow tube filled with sand to reduce mechanical vibrations. The upper removable end cap can house a six-axes load cell to collect force and torque data. Optical tachometers sense motor speeds, while precision shunt resistors measure electrical currents. Figure 1 shows the experimental setup while testing a quad-rotor vehicle and the combined thrust coefficient of the four rotors plotted against the Reynolds number and Mach number. We can appreciate a linear increase of the thrust coefficient with the Reynolds numbers up to about 120,000. Then an asymptotic behaviour is achieved. On the other hand, no clear trend is appreciated for this range of Mach numbers. Measurements on the propulsion system alone are possible by reconfiguring the test stand, as shown in the following section.

## C. Experimental tests on an isolated rotor

The experimental results of rotor performance tests carried out according to the procedure detailed in [18, 19] are reported in Fig. 2, which shows the thrust coefficient  $C_T$  versus the Reynolds number. We considered a T-Motor 15'x5' carbon fiber rotor due to the availability of geometrical details and experimental measurements in [10], which we can use for comparison. The experimental data in Fig. 2 reveal a linear relationship between  $C_T$  and the Reynolds number, with degradation of the thrust coefficient as the Reynolds decreases. At the highest values of the Reynolds numbers, it seems that  $C_T$  approaches asymptotic behavior. The thrust coefficient degradation could derive from the effect of delayed transition and the formation of separated flow regions that may reattach, creating laminar separation bubbles. Previous studies, such as in [6], mention the existence of a critical Reynolds number of 120,000, below which the effects of laminar separation become significant and very sensitive to operating conditions that might affect transition. Above these limits, rotor performance shows an asymptotic behavior. That observation is in good agreement with our experimental results, as in Fig. 2d, where the figure of merit shows an almost linear increase with increasing Reynolds numbers until about  $Re=120,000$ , where an asymptotic evolution starts. Our CFD results using a transition model



(a) Thrust coefficient vs Reynolds number (quad-rotor tests)



(b) Thrust coefficient vs Mach number (quad-rotor tests)



(c) Quad-rotor testing in terraXcube

**Fig. 1** Experimental testing in terraXcube laboratory

are in good agreement with the trends of the non-dimensional coefficients that characterize rotor performance. A detailed explanation of the CFD model employed to obtain such results and quantitative comparison between numerical and experimental results will follow in section III. Concerning the comparison with experimental data provided by Russel et al.[10], the asymptotic value of thrust and torque seems to be in good agreement also. However, there is a slight overestimation of thrust and torque values for the lowest Reynolds numbers. Despite such overestimation, the performance degradation is again in good agreement if we observe the figure of merit. The reasons for these discrepancies are currently under investigation. They are probably related to the different experimental procedures and also to the extremely high sensitivity of laminar separation bubbles to free stream conditions as reported in [22].

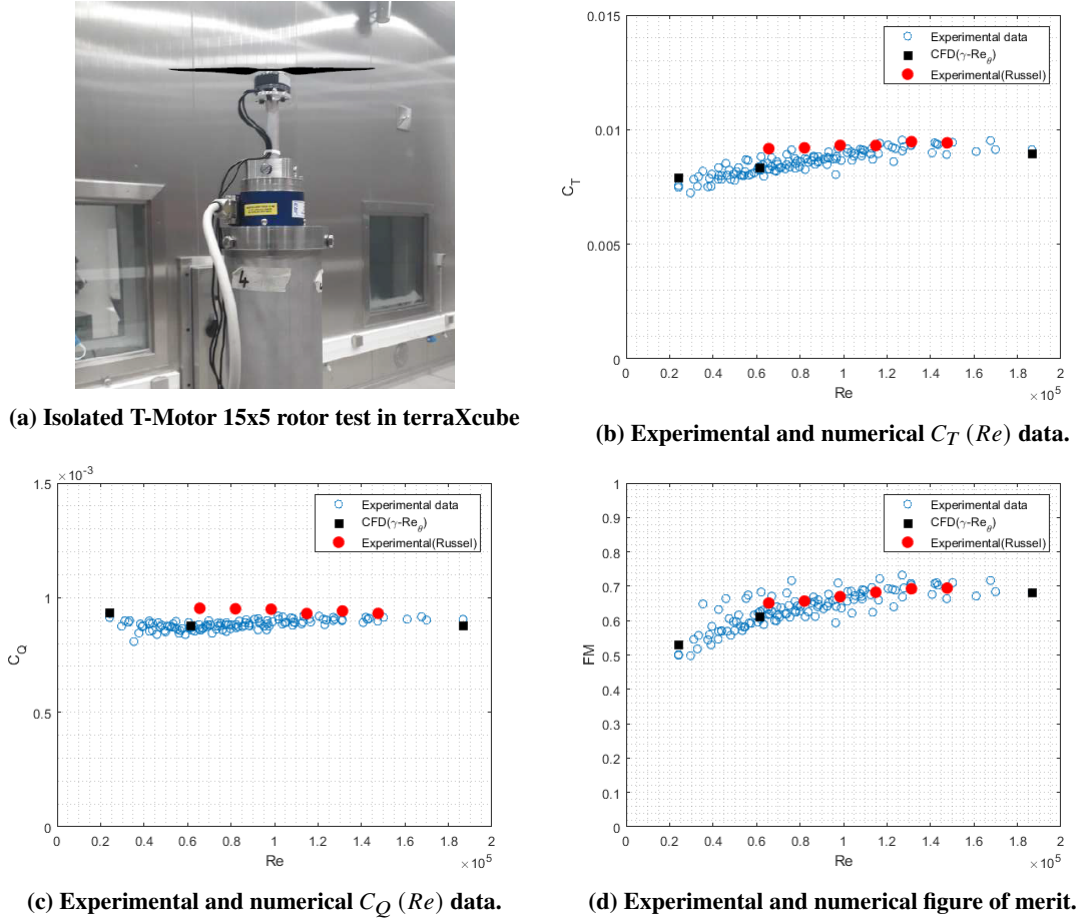


**Fig. 2** Experimental measurements (terraXcube and [10]) and numerical results for an isolated rotor.

### III. CFD simulations on isolated rotors

#### A. Blade geometry

We analyzed the T-motor 15x5 CF two-bladed rotor using an optical precision measuring machine (OPMM) to obtain an accurate three-dimensional model for CFD simulations. The 3D scan of the blade generated a cloud of points



defining the outer surface. We sliced the cloud of points with planes normal to the radial direction with a step of 1 cm to reproduce an accurate geometry. We interpolated the intersection points with a smooth spline, and we generated a guiding curve using the points defining the leading edge. A lofting process allows generating a smooth manifold surface, which is appropriate for CFD simulations. Figure 3 shows the top and front views of the reconstructed geometries (right) compared with images of the original rotor (left).



**Fig. 3 Comparison of top and front views of the original (left) and digitally reconstructed (right) blade.**

## **B. Model description and assumptions**

We performed numerical experiments using the commercial CFD software STARCCM+[23]. It is possible to simulate the rotational motion either with a rotating grid incorporating the rotor, the so-called dynamic or sliding mesh approach, or using a rotating reference frame to which the rotor is stationary, the Moving Reference Frame (MRF) technique. In the latter approach, the grid is static, and the effect of rotation depends on source terms inserted into the conservation equations, which introduce the Coriolis and centripetal acceleration. Various authors have validated the MRF approach [24–27], reporting a good agreement between approaches. The MFR approach is well suited to steady-state solution methods, which normally reduce the computational cost significantly compared to time-accurate analyses. Unfortunately, the approach is only accurate when the flow on the side surface of the cylinder defining the rotating region is nearly tangent to it[23, 28], and one must therefore be cautious in defining and meshing these areas. The static nature of the MRF approach allows for straightforward use of the transition model  $\gamma\text{-Re}_\theta$ . This transition model has been previously used to capture transition in rotating flows, namely in a wind turbine [29] and in a marine propeller [25]. The  $\gamma\text{-Re}_\theta$  model is highly empirical and depends upon three correlations that have been published in slightly different forms by various authors [30, 31]. In this paper, we use the correlations provided in [30]. The dynamic approach uses a cylindrical mesh that rotates about its axis and whose contours lap a static external domain. The dynamic approach is more general than the MFR approach. For this reason, it is the ideal choice when transient effects are important and when symmetry conditions are inapplicable. It is also helpful when the rotating domain cannot be large enough to reduce the artificial fluxes at the interface in the MFR method.

The numerical setup reproduces, in a simplified but consistent manner, the experimental arrangement in an attempt

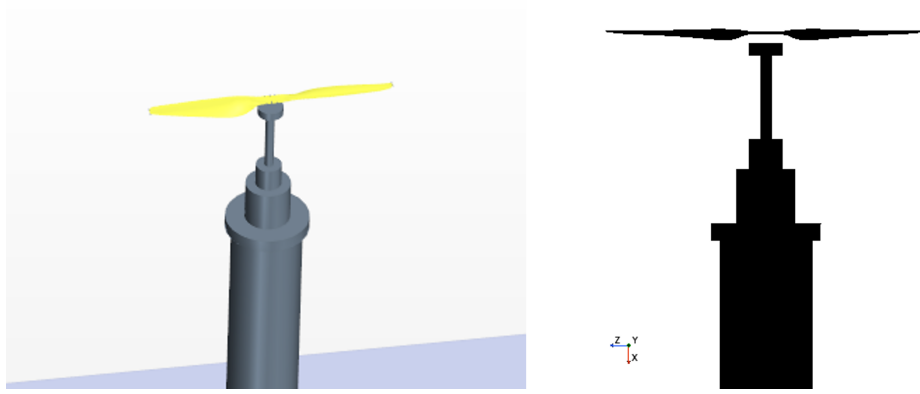


**Fig. 4 Numerical setup. Perspective view(Left) and parallel scaled view(Right)**

	Isolated Rotor		Experimental fixture	
Reynolds number	Thrust [N]	Torque [Nm]	Thrust [N]	Torque [Nm]
186,670	12.85	0.243	13.04	0.244

**Table 2 Numerical results on the effect of support on the rotor thrust and torque coefficients (MRF approach and Adaptive Mesh Refinement).**

to account for the possible blocking effect of the pole, which has a diameter comparable to that of the propeller as shown in Fig. 4. Previous studies [27] suggest that the blocking effect with similarly sized experimental equipment can produce significant increases in thrust and torque of up to 5% and 2%, respectively. Here, for the highest Reynolds number, we found just an additional 1.5% and 0.5% in the thrust and torque values, respectively, as shown in Table 2. The limited increase in thrust and torque could be due to the extra rod present in our simulations (Figs. 1c and 2a) that was not present in the simulations reported in [27].

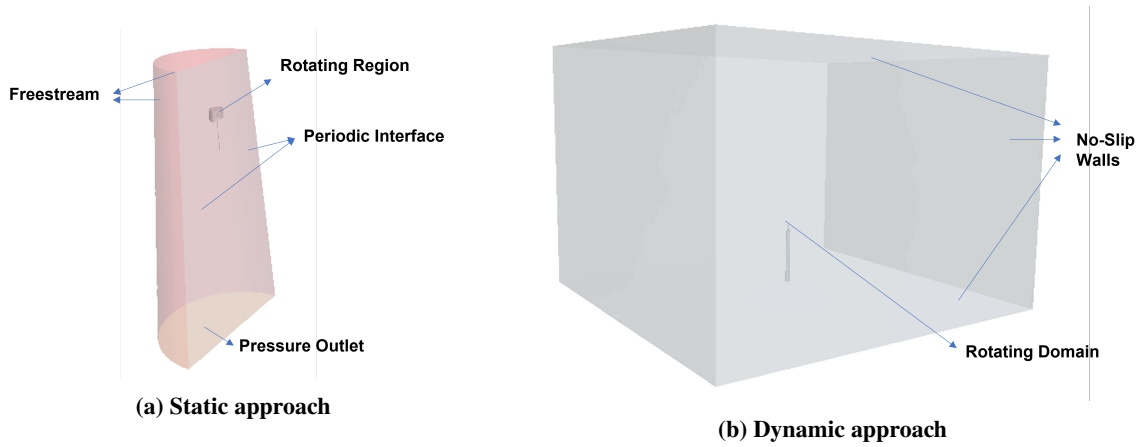


**Fig. 5 Boundary conditions**

Regarding boundary conditions, the setup differs between static and dynamic approaches as shown in figure 5. In the latter, we created a box that imitates the dimensions of the actual chamber using wall boundary conditions. In the MFR approach, we used a long, truncated, cone-shaped domain with free stream conditions characterized by a minimal axial velocity (0.1 m/s) to speed up convergence and a pressure outlet. The rotor is placed 2 meters ( $>5$  diameters) above the ground so that ground effect should be negligible [19] and hence both simulations should be comparable.

### C. Turbulence and transition modelling

We chose the SST  $k - \omega$  turbulence model as it is probably the most widely used for external aerodynamics and has been proven effective in propeller simulations by several authors [24, 28, 32]. Furthermore, it allows the coupling with the  $\gamma$ - $\text{Re}_\theta$  transition model to adequately capture laminar to turbulent transition and hence the formation of laminar separation bubbles as shown in [33]. The ability to include a transition model is interesting because, if the model works, one could resolve both laminar and turbulent boundary layers. We applied a laminar flow model for the lowest Reynolds numbers, as large portions of the blade might be in laminar flow conditions. Perez Perez [34] took the same approach to calculate the aerodynamic database for a reduced-order model. Table 3 shows an increase in the accuracy of the thrust prediction when the transition model is activated, with an error reduction by approximately 45% for the highest Reynolds number. Furthermore, as we show in the following section, the inclusion of the transition model triggers two different transition mechanisms, which bring to the generation of a laminar separation bubble. In this way, the near-blade flow field is qualitatively more accurate than using a standard turbulence model for these very-low Reynolds numbers. It is interesting to note that the torque remains constant. This result is due to a combination of increased pressure torque and decreased shear torque. In this particular case, an exact cancellation is produced. The previous observation is consistent with an increase in blade lift and a decrease in blade drag.

Reynolds number	CFD simulation			CFD vs. Experimental data	
	Turbulence model	Thrust [N]	Torque [Nm]	$\Delta$ Thrust %	$\Delta$ Torque %
186,670	$k - \omega$	12.74	0.244	-5.00	-3.71
186,670	$k - \omega + \gamma\text{-Re}_\theta$	13.04	0.244	-2.76	-3.71

**Table 3** Experimental vs numerical results. MRF approach, Adaptive Mesh Refinement, SST  $k - \omega$  turbulence model with and without transition model

### D. Grid independence study

Accurately resolving tip vortices, at least until they first interact with the blade, is crucial, especially in hovering cases where the vortices are very close to the propeller, and the velocity they induce on the rotor is relevant[35]. Vortex cores require a much smaller cell size than the rest of the flow field. However, a standard refinement strategy involving

the entire computational domain, or even the wake region only, increases the number of cells prohibitively before achieving grid convergence. Here we adopted various mesh refinement strategies starting from a baseline grid (Fig. 6) and increasing the number of cells where we expect strong gradients, as in tip vortices and the propellers' near wake.

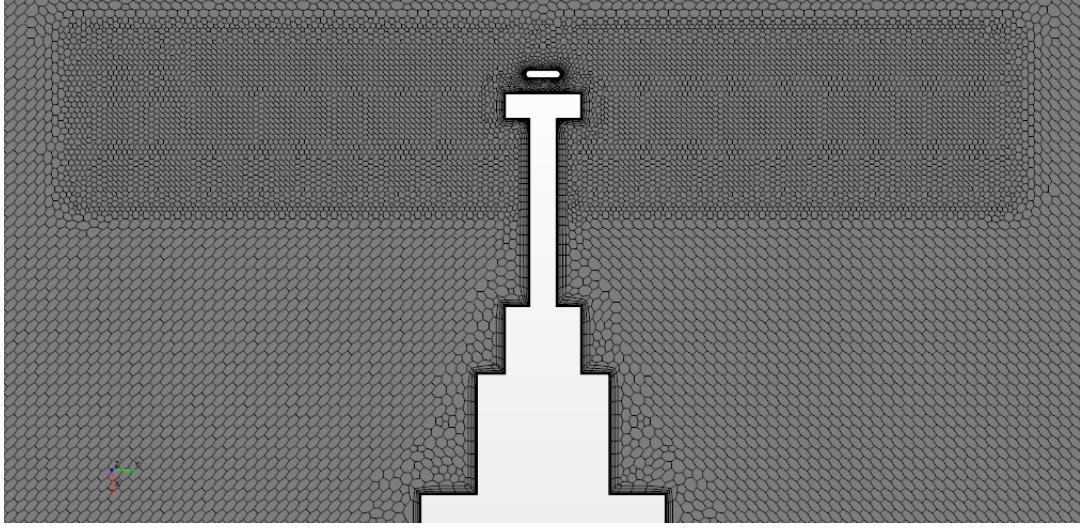


**Fig. 6 Baseline Grid.**

Using the MFR approach, we applied an adaptive grid refinement based on the Q-criterion to correctly track and resolve tip vortices, as shown in Fig. 7. Based on this experience, in the dynamic approach, we axisymmetrically refined those

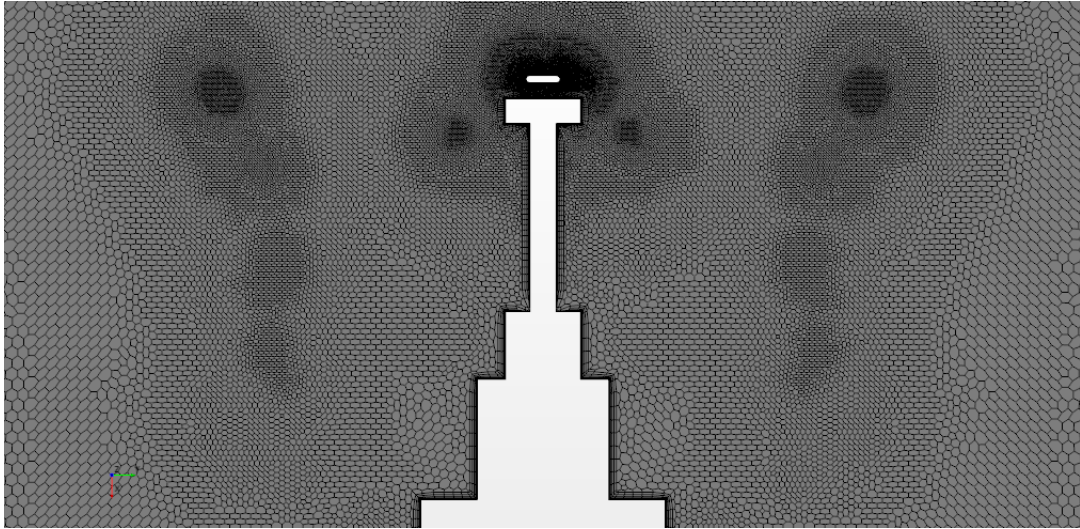
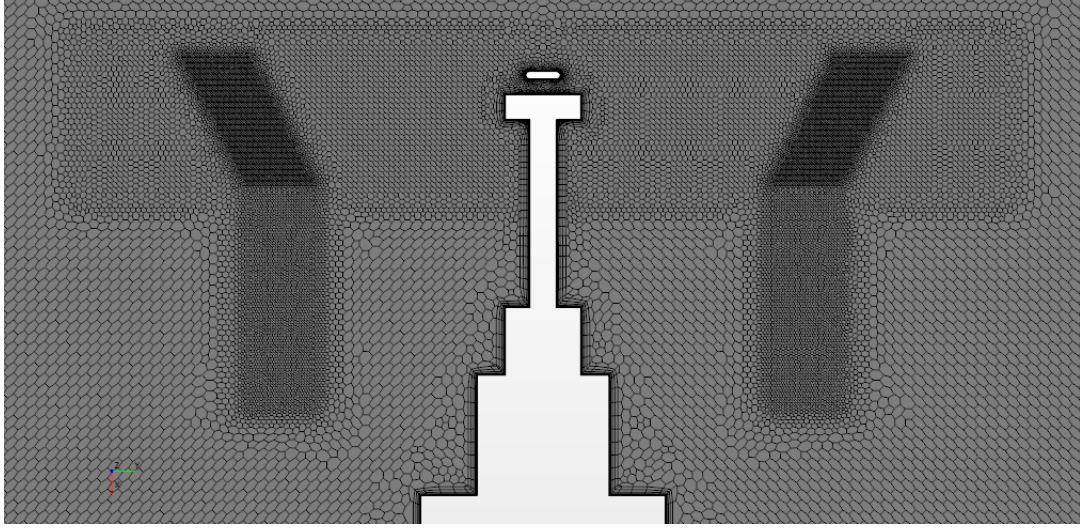


**Fig. 7 Adaptive Mesh Refinement (AMR) based on the Q-criterion. MRF approach.**

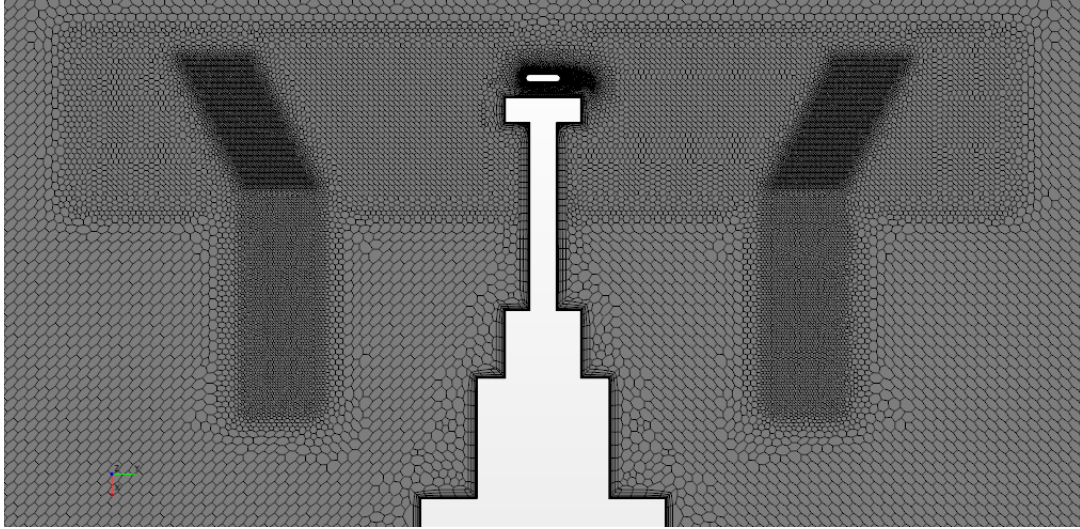
regions where we expect to see tip vortices, as shown in Fig. 8. We further refined the grid by reducing the target cell size on the propeller surface, increasing the number of prism layers, and adding a wake refinement near the trailing edge of the blades, as shown in Fig. 9.

Table 4 summarizes the three adopted refinement levels and highlights how the local refinement produced significant





**Fig. 8 Baseline Grid with tip vortex refinement.**



**Fig. 9 Baseline Grid with tip vortex and near rotor refinement.**

improvement in the comparison between numerical and experimental results using a limited number of cells for the highest Reynolds number condition. We considered such case as it was likely to present the steepest gradients and, therefore, require the highest number of cells to achieve grid convergence. Furthermore, at these Reynolds numbers, the transition model is expected to perform better, and therefore the comparison with the experimental results will be more realistic. The grid size would have easily reached 100 million cells had we used a global refinement strategy. In these simulations, showing a traditional grid convergence study based on systematic global mesh refinement/coarsening is impossible due to the limited computing capabilities. However, the intense, localized refinement and the reasonably small distance from the experimental measurements suggest that grid convergence is not far. The finest grid will be used in the results presented in the following chapter.

CFD simulation				CFD vs. Experimental data	
Grid	N° Cells	Thrust [N]	Torque [Nm]	$\Delta$ Thrust %	$\Delta$ Torque %
Baseline	8.6 Million	13.03	0.238	-2.83	-5.29
Tip vortex	14.1 Million	13.13	0.241	-2.09	-4.89
Tip vortex & Propeller	17.0 Million	13.16	0.246	-1.86	-2.92

**Table 4** Grid refinement study using the dynamic approach at  $Re=186,670$

### E. Comparison between the MRF and the dynamic approaches

We compared the performance prediction capabilities and computational cost of the static (MRF) and dynamic approaches in the highest Reynolds number case. Both simulations use the baseline grid settings shown in Fig. 6. The two meshes are not identical because the computational domains are different. However, the baseline grids are the same in the region near the rotor and should allow a fair comparison of the results of the two approaches. Table 5 shows how the performance results predicted by both approaches, using the same turbulence modeling and the baseline grid, are very close. It could indicate that the nonstationarity in the averaged flow is low, and therefore the steady MFR approach reproduces well the rotational motion of a propeller. The introduction of source terms in momentum equations might compromise convergence, and therefore one should carefully select the solver settings and cautiously build the grid. In the static approach, we consider just one blade using a periodic boundary condition, and therefore the cell count is halved. Adding this characteristic to the faster convergence rate of the steady approach reduces the computational cost by approximately a factor of 6. We used a conservative time step equivalent to a rotation of  $0.5^\circ$  to ensure time accuracy even though other studies use larger values [36]. In particular [36] finds an error of 1.6% increasing the angular advance per time step from  $0.5^\circ$  to  $3^\circ$ .

Finally, we compared the results obtained using the grids that provide the closest values to the experimental results using both approaches, namely the baseline grid with tip and near rotor refinement (Fig. 9) for the dynamic mesh and the AMR grid (Fig. 7) for the MFR approach. Table 6 shows that thrust and torque differ by less than 1% for two operating conditions even by changing the mesh, the solver, and the rotation methodology. Another conclusion extracted from this study is the high efficiency of the AMR grid combined with a periodic interface that can provide comparable results with one-third of grid points and reduce the total computational time by a factor of 10. Such methodology is

	Static approach		Dynamic approach	
Reynolds number	Thrust [N]	Torque [Nm]	Thrust [N]	Torque [Nm]
186,670	13.14	0.238	13.03	0.240

**Table 5** Comparison between static and dynamic approaches using baseline grids

noticeably helpful for propeller characterization as one can obtain the values of the integral performance parameters of the rotor with satisfactory precision.

	Static approach		Dynamic approach	
Reynolds number	Thrust [N]	Torque [Nm]	Thrust [N]	Torque [Nm]
61,539	4.08	0.0830	4.12	0.0828
186,670	13.04	0.244	13.16	0.246

**Table 6** Static (AMR mesh) vs dynamic (baseline grid with tip vortex and near rotor refinement) approach

## F. Results

We compare our experimental measurements and numerical results obtained using the dynamic approach and the 17 million cell grid for three representative Reynolds number conditions in Table 7. We discuss the main flow features in the following subsections.

	CFD simulation			CFD/Experimental data %	
Reynolds number	Turbulence model	Thrust [N]	Torque [Nm]	$\Delta$ Thrust %	$\Delta$ Torque %
24,099	Laminar	1.21	0.0280	-4.27	-4.76
24,099	$\gamma$ - $Re_\theta$	1.33	0.0299	5.22	1.70
61,539	$\gamma$ - $Re_\theta$	4.12	0.0828	-0.96	0.98
186,670	$\gamma$ - $Re_\theta$	13.16	0.246	-1.86	-2.92

**Table 7** Experimental data vs CFD simulations. Dynamic approach, 17 million cells.

### 1. $Re=24,099$

For the lowest Reynolds number, we initially performed a laminar simulation. Figure 10 shows a Q-criterion iso-surface that reveals, apart from the expected rotor vortex system formed by pairs of root and tip vortices, noticeable vortex shedding towards the tip of the blade. Table 7 shows that the laminar solver underestimates thrust and torque values by under 5%. The results look promising considering the absence of turbulence models. At these Reynolds numbers, the vortex shedding pattern is likely to become turbulent, so we rerun the simulation using the  $\gamma$ - $Re_\theta$  transition model, even though it was not clear if the transition model would work adequately for Reynolds numbers as low as 24,000. The results show that the separated boundary layer undergoes transition, but the production of turbulent kinetic energy is not fast enough to produce boundary layer reattachment before the trailing edge. However, since the transition model calibration arises from two-dimensional boundary layer simulations, the reliability of the transition process predicted after the trailing edge is at least doubtful. Using the  $\gamma$ - $Re_\theta$  transition model, thrust and torque are overpredicted by 5%

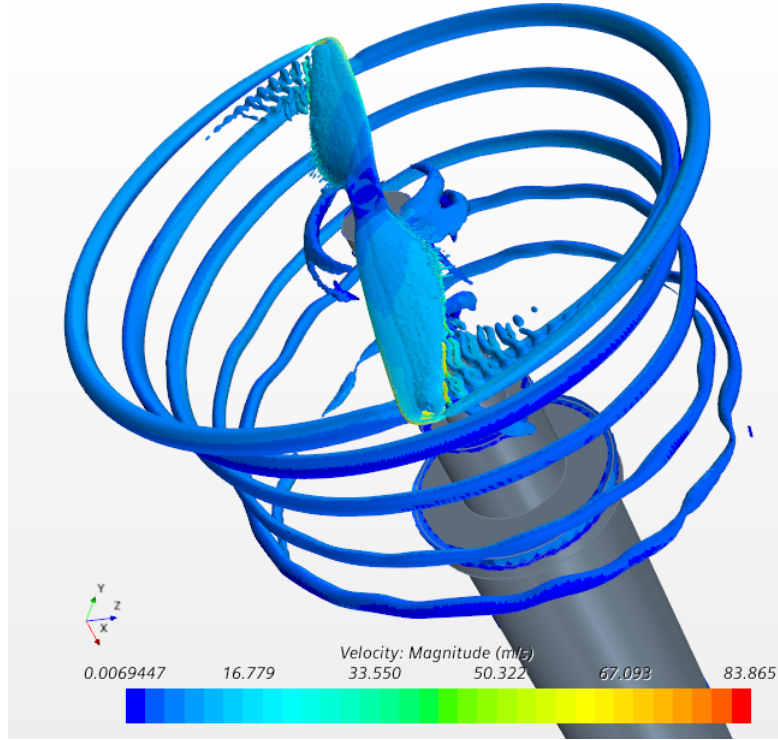


**Fig. 10 Q-criterion iso-surface coloured with velocity magnitude.  $Re=24,099$ .**

and 2%, respectively. Even though the difference with the experimental measurement is limited, the validity of this empirical transition model could be compromised for these and especially for lower Reynolds numbers, as this model has been designed, tuned, and tested mainly for flat plate cases at higher Reynolds numbers[29, 30]. The spatial and temporal resolution required to capture the vortex shedding in laminar simulations with sufficient accuracy is currently under investigation. However, the laminar solver could become an attractive option to compute the performance of blades in the lower range of the very-low-Reynolds number regime ( $10^4 - 10^5$ ), as, in these conditions, the effects of turbulence in the averaged flow are modest, and the transition model reliability is questionable.

## 2. $Re=61,539$

We chose to perform a numerical experiment at this Reynolds number because we expected to find a laminar behavior in the inner region of the blade and transition towards the tip. Transition models such as the  $\gamma-Re_\theta$  model are highly empirical, and their calibration relies mainly on 2D boundary layer simulations. Nevertheless, they should identify the main transition mechanisms. At these Reynolds numbers, separation usually triggers the transition, as shown by [37, 38] for the SD7003 airfoil using scale resolving simulations. If separation induced transition is captured, they should also detect the separation bubbles formed after the reattachment of the boundary layer due to the increased near-wall momentum of the now turbulent boundary layer. Figures 11a and 11b show different wall quantities that



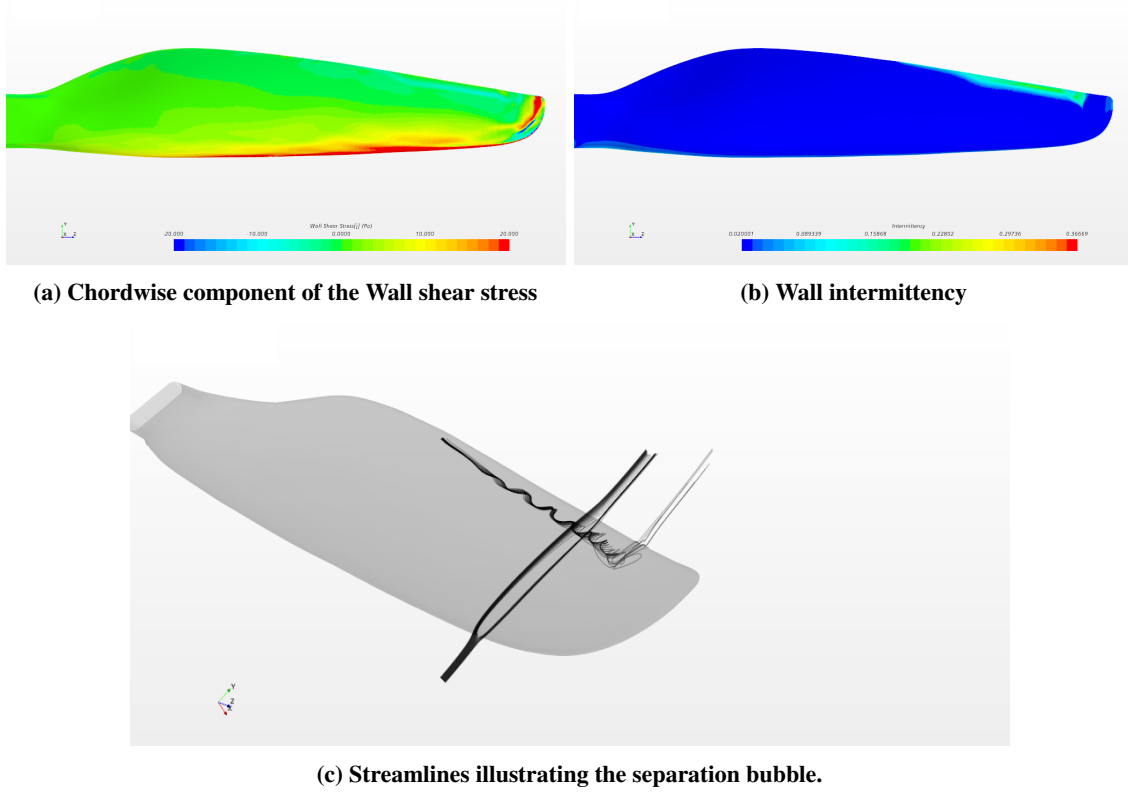


**Fig. 11 Near blade fluid flow characteristics.  $Re=61,539$**

could help identify the presence of a separation bubble on the suction side of the blade. The separated flow region followed by a rise in intermittency suggests the formation of a separation bubble as corroborated by the streamlines shown in Fig. 11c which we computed using the velocity expressed in the rotating reference frame. Apart from the expected recirculation, one can notice a velocity component directed towards the blade tip. That is due to the lack of centripetal forces when the wall shear stress is low, and its effect is producing a spiral motion towards the blade tip in the streamlines trapped inside the separation bubble.

### 3. $Re=186,670$

This value of the Reynolds number is the largest in the experimental matrix. Here transition is expected, though it has not to be necessarily separation-induced but likely natural, as the local Reynolds number is almost 200,000 in the outer part of the blade. Figure 12 shows a separated region with posterior transition and reattachment of the boundary layer between 50% and 60% of the blade span. Separation is no longer present for larger radial coordinates, but natural transition still occurs. Furthermore, towards the tip, possibly due to the large relative thickness of the airfoil's leading-edge, we can notice a separation again, followed by a noticeable increase in wall shear stress which indicates the presence of a short, leading-edge separation bubble.

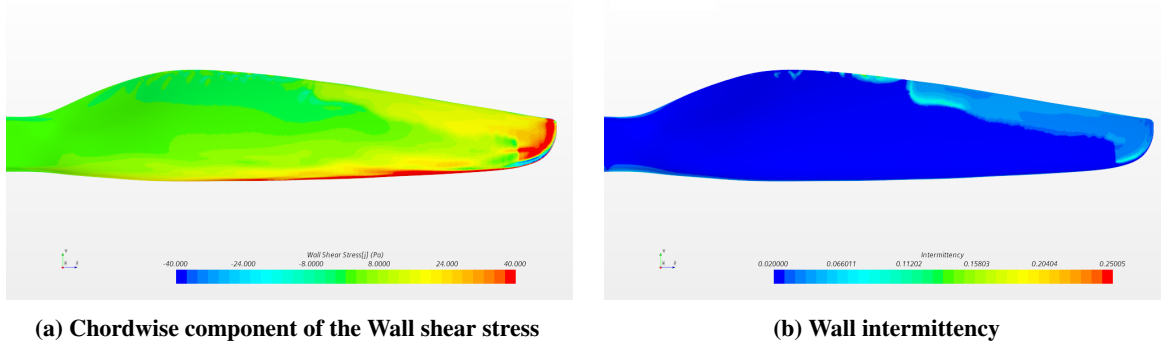


**Fig. 12 Near blade fluid flow characteristics.  $Re=186,670$**

#### IV. CFD simulations on a quadcopter

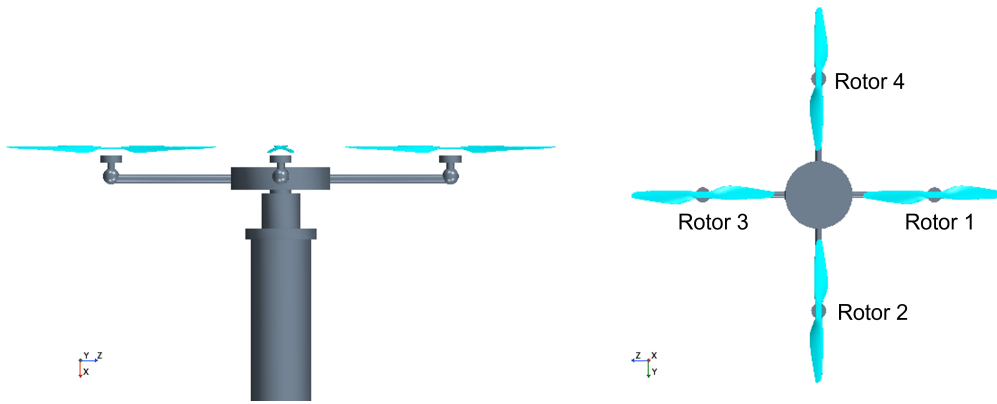


**Fig. 13 Numerical setup of the complete quadcopter.**

In the previous section, we validated the rotation model, and now we use it to simulate the full quadrotor. We constructed a simplified CAD model compliant with the original Q4L drone to assess the download effect on the thrust coefficient due to the rotor-rotor interactions. The Q4L mounts four Tmotor 15'x5' rotors, the tested blade in the previous section. The numerical setup is shown on figure Fig. 13. We performed a simulation with four rotors, each one with its own experimentally measured rotation speed, for the highest Reynolds number case ( $Re=181,410$ , Fig. 1a). This Reynolds number is obtained using the average RPM shown on Table 8 in combination with a temperature of 233.8 K and a pressure of 98,280 Pa. The results are a reference solution that we compare with results obtained using a single rotor with symmetry boundary conditions. Conversely, in the simulations adopting the symmetry boundary conditions, the rotation speed of the unique rotor is set as the root-mean-square value of the four rotation rates shown in Table 8. Figure 14 displays the mesh around the complete quadcopter, which consists of 46 million cells. The symmetry boundary condition simulation uses a grid with approximately one-quarter of the cells compared to the four rotors case. The simulation setup is consistent with the isolated rotor simulations proposed in the previous chapter. Table 9 and Fig. 15 show that the simulations using the symmetry boundary condition provide almost identical results even

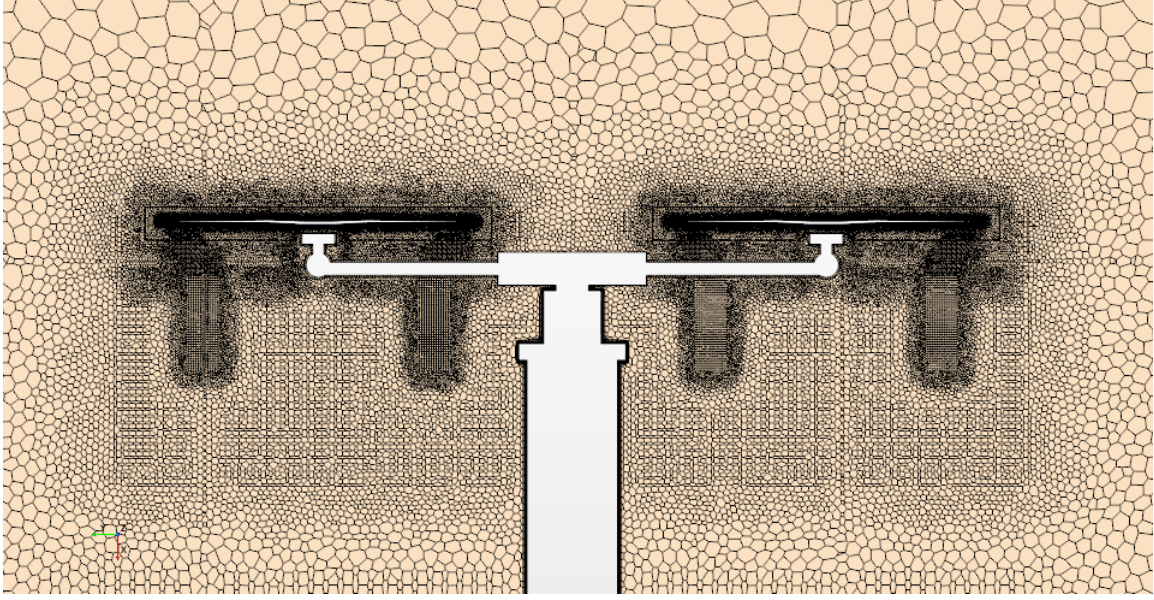


**Fig. 14 Grid around the complete quadcopter.**

though the physical problem is not the same as the rotation rates are slightly different. The reduced vortex breakdown suggests that the symmetry boundary condition dampens rotor-rotor interactions slightly for this rotor separation distance. However, the thrust value looks virtually unaffected by this phenomenon and applying the symmetry boundary conditions reduces the simulation time and the memory requirements by a factor of 4. It is interesting to note that the rotor-rotor interactions are more intense in the inter-rotor planes when the tip of the blades moves from the center of the vehicle outwards, as one can see in Fig. 15. In particular, the images in Figs. 15b–15d represent the same situation as Figs. 15a–15c, respectively, but we rotated them by  $90^\circ$  to highlight the different planes of interaction. Fig. 16 shows how a pair of counter-rotating vertical vortices are created in the inter-rotor region near the smallest tip clearance location. We can appreciate that these vortices only appear in the previously defined strong rotor-rotor interaction planes. These vortices are responsible for the enhanced breakdown of the rotor tip vortices seen in Fig. 15. Schenk [36] observed that two counter-rotating isolated rotors induce a local upwash current in the inter-rotor regions following the direction in which the tips move. On the other hand, the vortex system generated by the four rotors induces a radial current towards the centre of the quadcopter in these planes. When the tips move towards the body, both currents move in the same direction, but when they move away from the body, the induced currents oppose each other. The authors believe that this is the cause of the vortices formation. However, further research is needed to understand in detail the mechanism of this instability.

To assess the effects of rotor-rotor and rotor-body interactions on the integral vertical force on the quadrotor, we computed the thrust coefficient using the average rotation speed for the complete vehicle. Then, we compare it to the corresponding isolated rotor at the closest Reynolds number. Equation (1) shows the relation to calculate the download

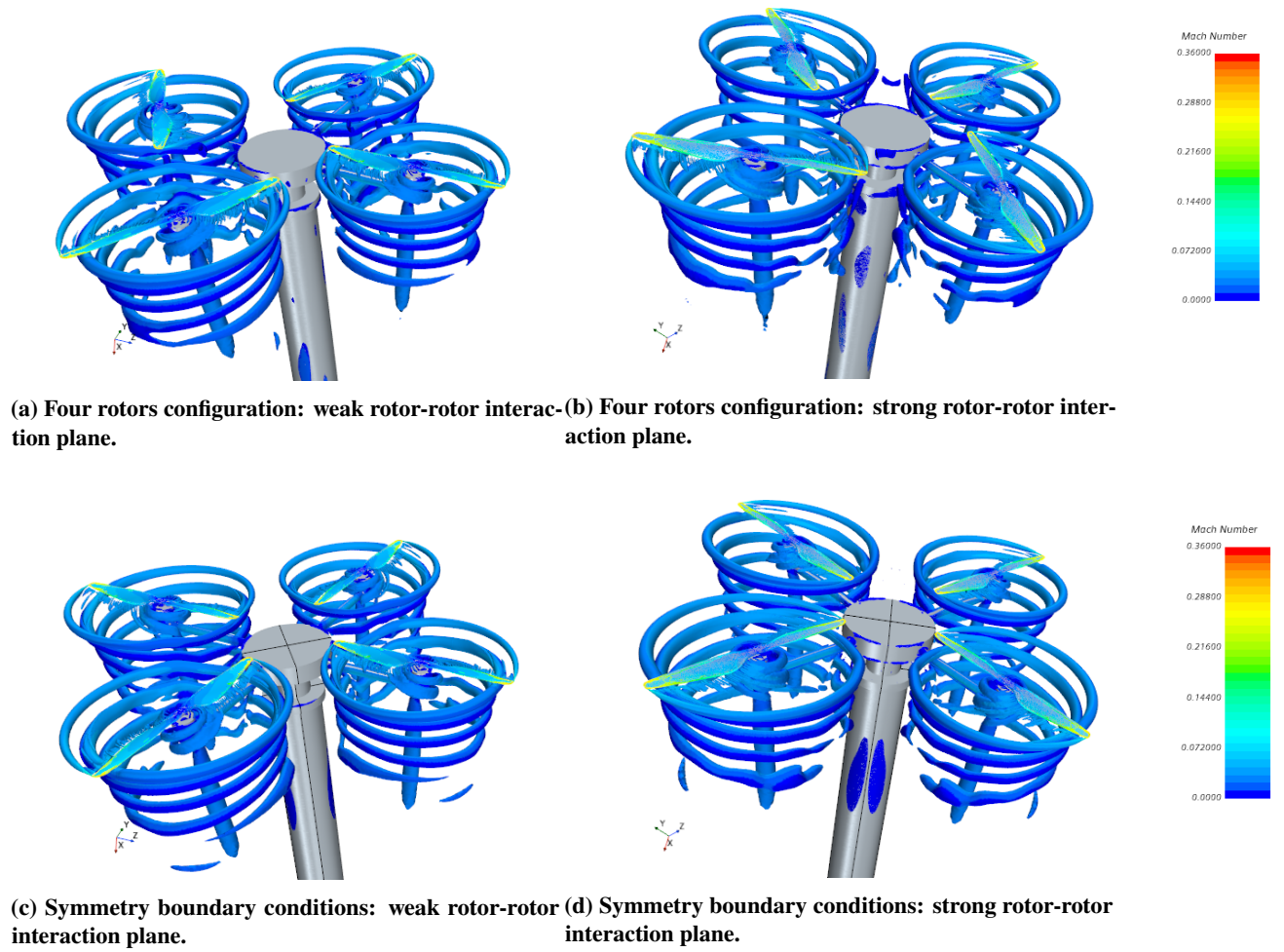


Fig. 15 Q-criterion coloured with Mach number around the quadcopter including experimental fixture.

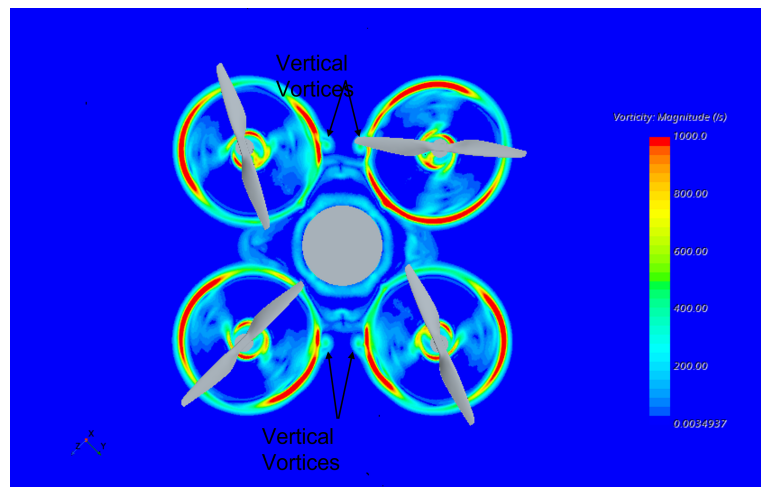


Fig. 16 Vorticity magnitude in a horizontal plane  $x=0.02\text{m}$ .

factor, which takes into account the overall decrease in the axial force of a quadcopter due to the interaction between rotors and airframe.

RPM Rotor 1	RPM Rotor 2	RPM Rotor 3	RPM Rotor 4	Mean RPM	Root Mean Square RPM
4338	4310	4388	4316	4338	4338

**Table 8** Rotation rates of the four rotors in the full quadcopter configuration.

$$DL = \frac{4C_{T_{rotor}} - C_{T_{UAS}}}{4C_{T_{rotor}}} \quad (1)$$

	Symmetry Condition	Full Quadcopter	Experimental
Mean RPM	4 x Thrust [N]	Thrust [N]	Thrust [N]
4338	42.72	42.65	44.2

**Table 9** Comparison between experimental and numerical approaches to compute the quadcopter thrust.

The highest Reynolds number conditions for the isolated rotor ( $Re=186,670$ ) are close to the quadcopter ( $Re=181,410$ ) and therefore allow a reasonable comparison between thrust coefficients. The download factor computed numerically provides a value of 4.5% compared to the experimental 3%. One possible explanation for this difference is the lack of resolution in the boundary layer and wake behind the quadcopter arms and body. Another one resides in the difficulties that RANS turbulence modeling encounters in accurately predicting drag values in separated flows. Of course, another explanation for the discrepancies might be attributed to minor geometrical simplifications introduced in the numerical model, namely in some details of the airframe.

## V. Conclusions and Future Work

In this paper, we report on a study on the aerodynamics of small-scale multicopters with both experimental and numerical approaches. On the one hand, we show the measurements of small rotor performance coefficients conventionally used in small-scale UAS for a set of flight conditions. On the other hand, we report about CFD numerical simulations intending to define a suitable protocol, especially about grid resolution and turbulence modeling, to describe low Reynolds number effects. Within the high transitional regime, the use of the  $\gamma-Re_\theta$  transition model[39] with the calibration proposed by [30] produces a satisfactory agreement for both the tested Reynolds numbers in this regime, 61,539 and 186,670. Therefore, we expect that it performs correctly within this range ( $60,000 < Re < 200,000$ ). For the low transitional regime, the performance predictions with the transition model start to deviate from the experimental results. That is not surprising, as the values of the Reynolds number are close to the onset of transition and well below

the design and calibration regime of the transition model. In such conditions, the laminar solver might be advantageous to compute rotor performances for Reynolds numbers lower than 20,000, when the transition does not occur, or when its effect on the averaged flow is little and contained in a small blade portion.

We used the experimental data to validate CFD simulations and obtained a satisfactory agreement for all the Reynolds numbers. The use of localized meshing strategies, the inclusion in the geometric model of the experimental device, and precise blade geometry obtained by 3D optical scanning were instrumental in accurately reproducing the experimental results.

The validation of the Moving Reference Frame approach for rotor simulation in hovering is also interesting as it reduces the computational cost by approximately one order of magnitude compared to the dynamic approach while maintaining reasonable accuracy. This reduction in required computational resources allows the use of CFD simulation in optimization and design activities. Therefore, it would be possible to design rotor geometries to maximize performance, limiting the negative impact of low Reynolds number effects.

We also carried out full rotorcraft simulations, obtaining a satisfactory agreement with the experimentally measured thrust values. We just noted a slight overestimate of the download factor compared to the experimentally computed value, possibly due to a lack of grid resolution in the wake of the rotors arms and the loss of fidelity of RANS turbulence models when dealing with large flow separations.

Future work includes investigating the low-Re transitional regime with a twofold goal. The first is fine-tuning existing transition models to improve performance predictions, and the second is defining a validity range for the laminar model. The objective is to avoid turbulence-scale-resolving simulations that would be prohibitively expensive for practical applications. Furthermore, automatic AMR is currently under investigation to improve the computational efficiency of dynamic simulations by refining the grid in real-time following tip vortices and saving a considerable amount of cells, as already shown for the static AMR approach.

## Acknowledgments

The authors gratefully acknowledge the support and would like to thank the Quality and Metrology Laboratories of the Department of Management and Production Engineering (DIGEP) at Politecnico di Torino for the optical scanning of the rotor blades geometry.

## References

- [1] Balaram, B., Canham, T., Duncan, C., Grip, H. F., Johnson, W., Maki, J., Quon, A., Stern, R., and Zhu, D., “Mars helicopter technology demonstrator,” *2018 AIAA Atmospheric Flight Mechanics Conference*, Kissimmee, Florida, 2018. AIAA-2018-0023.
- [2] Blanks, M., “UAS Applications,” *Introduction to Unmanned Aircraft Systems*, edited by D. M. Marshall, R. K. Barnhart, E. Shappee, and M. Most, CRC Press, Taylor Francis Group, 2016, Chap. 2, 2<sup>nd</sup> ed.

- [3] Rakha, T., and Gorodetsky, A., “Review of Unmanned Aerial System (UAS) applications in the built environment: Towards automated building inspection procedures using drones,” *Automation in Construction*, Vol. 93, 2018, pp. 252–264.
- [4] Ackerman, K. A., Gregory, I. M., and Hovakimyan, N., “Flight Control Methods for Multirotor UAS,” *2019 International Conference on Unmanned Aircraft Systems (ICUAS)*, IEEE, Atlanta, GA, USA, 2019, pp. 353–361.
- [5] de Pierrepont, I. D. D. M., Carminati, D., Scanavino, M., Capello, E., et al., “Model-In-the-Loop Testing of Control Systems and Path Planner Algorithms for QuadRotor UAVs,” *2020 International Conference on Unmanned Aircraft Systems (ICUAS)*, IEEE, Athens, Greece, 2020, pp. 1809–1818.
- [6] Argus, F. J., Ament, G. A., and Koning, W. J., “The Influence of Laminar-Turbulent Transition on Rotor Performance at Low Reynolds Numbers,” *VFS Technical Meeting on Aeromechanics for Advanced Vertical Flight*, San Jose, Ca, USA, 2020.
- [7] Brandt, J. B., “Small-scale Propeller Performance at Low Speeds,” Master’s thesis, University of Illinois at Urbana-Champaign, 2005.
- [8] Brandt, J., and Selig, M., “Propeller Performance Data at Low Reynolds Numbers,” *49<sup>th</sup> AIAA Aerospace Sciences Meeting including the New Horizons Forum and Aerospace Exposition*, Orlando, FL, January 4-7, 2011. AIAA-2011-1255.
- [9] Russell, C., Jung, J., Willink, G., and Glasner, B., “Wind Tunnel and Hover Performance Test Results for Multicopter UAS Vehicles,” *AHS 72<sup>nd</sup> Annual Forum*, West Palm Beach, FL, May 16-19, 2016, pp. 1–20.
- [10] Russell, C. R., and Sekula, M. K., “Comprehensive Analysis Modeling of Small-Scale UAS Rotors,” *AHS International 73<sup>rd</sup> Annual Forum & Technology Display*, Fort Worth, TX, May 9-11, 2017, pp. 1–16.
- [11] Carreño Ruiz, M., Manavella, A., and D’Ambrosio, D., “Numerical and experimental validation and comparison of reduced order models for small scale rotor hovering performance prediction,” *AIAA SCITECH 2022 Forum*, 2022, p. 0154.
- [12] Alvarez, E. J., and Ning, A., “High-fidelity modeling of multirotor aerodynamic interactions for aircraft design,” *AIAA Journal*, Vol. 58, No. 10, 2020, pp. 4385–4400.
- [13] Ventura Diaz, P., and Yoon, S., “High-fidelity computational aerodynamics of multi-rotor unmanned aerial vehicles,” *2018 AIAA Aerospace Sciences Meeting*, 2018, p. 1266.
- [14] EURAC Research, “Climate in Cubes,” <https://terraxcube.eurac.edu/structure/>, 2020. Accessed: 2022-01-30.
- [15] Brugger, H., Brodmann, M., Turner, R., Nollo, A., Gatterer, H., and Strapazzon, G., “terraXcube: A new hi-tech training facility for EMS teams,” *Resuscitation*, Vol. 130, e79, 2018.
- [16] Niedrist, G., Nollo, A., Brugger, H., Vilardi, A., Leitinger, G., and Tappeiner, U., “terraXcube: An emerging ecotrone to converge chamber experiments and environmental studies in alpine ecology,” *Proceedings of the 20<sup>th</sup> EGU General Assembly, EGU2018*, Vienna, Austria, April, 4-13, 2018, p. 13616.

- [17] Scanavino, M., Vilardi, A., and Guglieri, G., “An Experimental Analysis on Propeller Performance in a Climate-controlled Facility,” *Journal of Intelligent & Robotic Systems*, Vol. 100, No. 2, 2020, pp. 505–517.
- [18] Scanavino, M., Avi, A., Vilardi, A., and Guglieri, G., “UAS testing in low pressure and temperature conditions,” *2020 International Conference on Unmanned Aircraft Systems (ICUAS)*, IEEE, Athens, Greece, 2020, pp. 1757–1765.
- [19] Scanavino, M., “Design and testing methodologies for UAVs under extreme environmental conditions,” Ph.D. thesis, Politecnico di Torino, 2021.
- [20] Scanavino, M., Avi, A., Vilardi, A., and Guglieri, G., “Unmanned Aircraft Systems Performance in a Climate-Controlled Laboratory,” *Journal of Intelligent & Robotic Systems*, Vol. 102, No. 1, 2021, pp. 1–16.
- [21] Glauert, H., “The effect of compressibility on the lift of an aerofoil,” *Proceedings of the Royal Society of London. Series A, Containing Papers of a Mathematical and Physical Character*, Vol. 118, No. 779, 1928, pp. 113–119.
- [22] McGhee, R. J., Walker, B. S., and Millard, B. F., “Experimental results for the Eppler 387 airfoil at low Reynolds numbers in the Langley low-turbulence pressure tunnel,” Tech. Rep. NASA-TM-4062, NASA, 1988.
- [23] Siemens, P., “STAR-CCM+ User Guide Version 14.06,” *Siemens PLM software Inc*, 2019.
- [24] Pawar, S., and Brizzolara, S., “Relevance of transition turbulent model for hydrodynamic characteristics of low Reynolds number propeller,” *Applied Ocean Research*, Vol. 87, 2019, pp. 165–178.
- [25] Webster III, J. A., “Design and Analysis of Low Reynolds Number Marine Propellers with Computational Fluid Dynamics (CFD) Transition Modeling,” Ph.D. thesis, Virginia Tech, 2019.
- [26] Potsdam, M. A., and Strawn, R. C., “CFD simulations of tiltrotor configurations in hover,” *Journal of the American Helicopter Society*, Vol. 50, No. 1, 2005, pp. 82–94.
- [27] Manavella, A., “Low Reynolds number propeller performance validation by CFD analysis and reduced order models,” Master’s thesis, Politecnico di Torino, 2021.
- [28] Carreño Ruiz, M., “CFD simulation of propellers: Best Practices Analysis,” Master’s thesis, Politecnico di Torino, 2019.
- [29] Langtry, R., Gola, J., and Menter, F., “Predicting 2D airfoil and 3D wind turbine rotor performance using a transition model for general CFD codes,” *44th AIAA aerospace sciences meeting and exhibit*, 2006, p. 395.
- [30] Langtry, R. B., and Menter, F. R., “Correlation-based transition modeling for unstructured parallelized computational fluid dynamics codes,” *AIAA journal*, Vol. 47, No. 12, 2009, pp. 2894–2906.
- [31] Malan, P., Suluksna, K., and Juntasaro, E., “Calibrating the  $\gamma - Re_{\theta}$  Transition Model for Commercial CFD,” *47th AIAA Aerospace Sciences Meeting*, Reno, NV, USA, 2009. AIAA-2009-1142.
- [32] Webster, J., Neu, W., and Brizzolara, S., “Reynolds Stress Transition Modeling for Marine Propellers at Low Reynolds Number,” *Sixth International Symposium on Marine Propulsors: Smp19*, Rome, Italy, 2019.



- [33] Carreño Ruiz, M., and D'Ambrosio, D., "Validation of the  $\gamma$ -Re  $\theta$  Transition Model for Airfoils Operating in the Very Low Reynolds Number Regime," *Flow Turbulence and Combustion*, 2022. <https://doi.org/10.1007/s10494-022-00331-z>.
- [34] Perez Perez, B. N., "Forward Flight Rotor Performance at Martian Atmospheric Densities and Sensitivity to Low Reynolds Numbers," *VFS Technical Meeting on Aeromechanics for Advanced Vertical Flight*, San Jose, CA, January 21–23, 2020.
- [35] Hariharan, N. S., Egolf, T. A., and Sankar, L. N., "Simulation of rotor in hover: Current state, challenges and standardized evaluation," *52nd Aerospace Sciences Meeting*, National Harbor, MD, USA, 2014. AIAA-2014-0041.
- [36] Schenk, A. R., "Computational Investigation of the Effects of Rotor-on-Rotor Interactions on Thrust and Noise," Master's thesis, Brigham Young University, 2020.
- [37] Uranga, A., Persson, P.-O., Drela, M., and Peraire, J., "Implicit large eddy simulation of transitional flows over airfoils and wings," *19th AIAA Computational Fluid Dynamics*, 2009, p. 4131.
- [38] Galbraith, M., and Visbal, M., "Implicit large eddy simulation of low-Reynolds-number transitional flow past the SD7003 airfoil," *40th fluid dynamics conference and exhibit*, 2010, p. 4737.
- [39] Menter, F., Langtry, R., and Völker, S., "Transition modelling for general purpose CFD codes," *Flow, Turbulence and Combustion*, Vol. 77, 2006, pp. 277–303.